Journal of Solid State Chemistry 182 (2009) 1177–1187

Contents lists available at ScienceDirect

Journal of Solid State Chemistry

journal homepage: www.elsevier.com/locate/jssc

Ab initio structure determination and Rietveld refinement of $Bi_{10}Mo_3O_{24}$ the member $n = 3$ of the $Bi_{2n+4}Mo_nO_{6(n+1)}$ series

J. Galy [a,*], J. Hernández-Velasco [b], A.R. Landa-Cánovas [b], E. Vila [b], A. Castro [b]

[a] Centre d'Elaboration de Matériaux et d'Etudes Structurales (CEMES-CNRS), 29, rue Jeanne Marvig, BP 94347, 31055 Toulouse, France
[b] Instituto de Ciencia de Materiales de Madrid (ICMM, CSIC), Cantoblanco, 28049 Madrid, Spain

ARTICLE INFO

Article history:
Received 16 October 2008
Received in revised form
14 January 2009
Accepted 6 February 2009
Available online 21 February 2009

Keywords:
Bismuth molybdenum oxide
Crystal structure
X-ray diffraction
Neutron diffraction

ABSTRACT

Bi_2O_3–MoO_3 system shows a large panoply of phases depending on Bi/Mo ratio, among them, the low temperature phases of the homologous series $Bi_{2(n+2)}Mo_nO_{6(n+1)}$ with $n = 3$, 4, 5 and 6. They exhibit, alike most of the phases of this system, strong fluorite sub-network. Nevertheless, a multitechnique approach has been followed in order to solve the crystal structure of the $n = 3$ member, i.e. $Bi_{10}Mo_3O_{24}$. From *ab initio* indexing X-ray powder pattern cell parameters were derived. It belongs to the monoclinic system, space group $C2$, with cell parameters: $a = 23.7282(2)$ Å, $b = 5.64906(6)$ Å, $c = 8.68173(9)$ Å, $\beta = 95.8668(7)^\circ$ with $Z = 2$. The matrix relating this cell with the fluorite one is $4\,0\,1/0\,1\,0/-\frac{1}{2}\,0\,\frac{3}{2}$ and a cationic localization was derived. HRTEM allowed the cationic Bi and Mo order to be modified and specified, as well as to build up a full structural *ab initio* model on the basis of crystal chemistry considerations. Simultaneous Rietveld refinement of multipattern X-ray and neutron powder diffraction data taking advantage of the neutron scattering length for O location have been performed. The goodness of the model was ascertained by low reliability factors, weighted $R_b = 4.97\%$ and $R_f = 3.21\%$. This complex $Bi_{10}Mo_3O_{24}$ structure, with 5Bi, 2Mo and 13O in different crystallographic positions of the asymmetric unit, shows good agreement between observed and calculated patterns within the data resolution. Moreover, the determination of this structure sets the basis for the crystallographic characterization of the complete family $Bi_{2(n+2)}Mo_nO_{6(n+1)}$, whose guidelines are also evidenced in this paper.

1. Introduction

In 2005, Vila and coworkers [1] showed the existence of a new phase, $Bi_{10}Mo_3O_{24}$ (mole ratio mBi_2O_3:$MoO_3 = 1.666$) belonging to the Bi_2O_3–MoO_3 system, which was prepared via wet-chemistry method and ulterior annealing at relatively low temperature, i.e. 600–750 °C. This phase transforms at higher temperature into a structure related to the columnar type of $Bi_{2/3}[Bi_{12}O_{14}](MoO_4)_5$, which exhibits a large homogeneity range in this system [2]. Single crystals of $Bi_{10}Mo_3O_{24}$ being not available, an automatic indexing based on X-ray powder pattern allowed to determine the crystal data of this phase which crystallizes in the monoclinic system; the cell parameters are $a = 23.7235$ Å, $b = 5.64720$ Å, $c = 8.6798$ Å and $\beta = 95.879^\circ$ and the selection rule for Miller indices gives the possible space groups $C2$, Cm or $C2/m$ [1]. From X-ray data the phase shows a strong sub-lattice of heavy atoms Bi and Mo and a matrix giving the relationship fluorite cell to $Bi_{10}Mo_3O_{24}$ was established i.e. $\{401/010/-\frac{1}{2}0\frac{3}{2}\}$. A tentative hypothesis about the heavy atoms distribution in the structure was proposed based on the marked contribution to the intensity of the peaks in the X-ray powder pattern. In this way, a reasonable agreement was obtained, although the structure solution had to be confirmed.

The development of chemical investigations on this Bi_2O_3–MoO_3 system showed the existence of three other phases, stable at such low temperatures: $Bi_{12}Mo_4O_{30}$, $Bi_{14}Mo_5O_{36}$ and $Bi_{16}Mo_6O_{42}$, corresponding to the molar ratios $m = 1.5$, 1.4, and 1.333, respectively. The cell parameters and space groups of these phases were also determined and it was concluded that all their structures were related to the fluorite structural type by a sub-cell matrix $\{(n+1)01/010/-\frac{1}{2}0\frac{3}{2}\}$, giving rise to the general formula $Bi_{2n+4}Mo_nO_{6(n+1)}$, with $n = 3$, 4, 5, 6 [3]. The crystal data of these phases are given in Table 1 and a scheme of these relationships for the various structures with the basic fluorite cell was depicted [3].

Studies of all these phases by electron diffraction have fully confirmed and established these first investigations, i.e. crystal system, parameters, space groups and matrices. A unified way to describe the reciprocal lattices was defined as $\mathbf{G} = h\mathbf{a}^* + k\mathbf{b}^* + l\mathbf{c}^* + m\mathbf{q}$; $\mathbf{a}^*$, $\mathbf{b}^*$, $\mathbf{c}^*$ being a basis of the reciprocal lattice, m an integer number and $\mathbf{q}$ a modulation vector defined as $\mathbf{q} = 1/13(602)^*$ for $n = 3$, $1/16\ (602)^*$ for $n = 4$, $1/19(602)^*$ for $n = 5$ and $1/22(602)^*$ for $n = 6$ [3].

* Corresponding author. Fax: +33 05 62 25 79 99.
E-mail address: galy@cemes.fr (J. Galy).

0022-4596/$ - see front matter © 2009 Elsevier Inc. All rights reserved.
doi:10.1016/j.jssc.2009.02.010

Table 1
Crystal data and relationships with fluorite sub-cell parameters for the series $Bi_{2n+4}Mo_nO_{6(n+1)}$ together with related phases.

Data	γ(H) Bi_2MoO_6	$Bi_7AsMo_3O_{21}$	$Bi_6Cr_2O_{15}$	$Bi_{2/3}Bi_{12}Mo_5O_{34}$ HT ($m = 1.267$)	$Bi_{16}Mo_6O_{42}$ LT $n = 6$ ($m = 1.333$)	$Bi_{14}Mo_5O_{36}$ LT $n = 5$ ($m = 1.400$)	$Bi_{12}Mo_4O_{30}$ LT $n = 4$ ($m = 1.500$)	$Bi_{10}Mo_3O_{24}$ LT $n = 3$ ($m = 1.666$)
System	Monoclinic	Monoclinic	Orthorhombic	Monoclinic	Monoclinic	Monoclinic	Monoclinic	Monoclinic
Space group	$P2_1/c$	$P2_1/n$	Ccc2	$P2/a$	$P2_1/a$	$C2$	$P2_1/a$	$C2$
a (Å)	17.2440(6)	12.777(1)	12.30184(5)	24.734(9)	39.97(2)	34.476(2)	29.0674(4)	23.7282(2)
b (Å)	22.4290(8)	5.5890(4)	19.87492(7)	5.801(3)	5.632(4)	5.6414(3)	5.64795(7)	5.64906(6)
c (Å)	5.5860(1)	27.971(2)	5.88162(2)	11.792(6)	8.634(4)	8.6433(4)	8.6620(1)	8.68173(9)
β (deg)	90.486(2)	101.01(1)		102.83(3)	101.02(2)	99.69(1)	97.98(1)	95.8668(7)
V (Å^3)	2160.4(2)	1960.7(3)	1438.0(1)	1665(3)	1907.6(2)	1657.1(1)	1408.3(2)	1157.62(1)
Z	16	2	4	2	2	2	2	2
$\rho_{exp.}$(g cm^{-3})	7.48(2)	7.04(4)	7.35(3)	7.36(3)	7.94(1)	7.98(3)	8.01(2)	7.90(1)
ρX (g cm^{-3})	7.500	7.096	7.380	7.389	7.981	7.982	7.960	7.926
Fluorite	3 0 0	2 0 −1	2 0 0	4 0 2	7 0 1	6 0 1	5 0 1	4 0 1
Sub-cell	0 4 0	0 1 0	0 4 0	0 1 0	0 1 0	0 1 0	0 1 0	0 1 0
Matrices	0 0 1	1 0 5	0 0 1	$-\frac{3}{2}0\frac{3}{2}$	$-\frac{1}{2}0\frac{3}{2}$	$-\frac{1}{2}0\frac{3}{2}$	$-\frac{1}{2}0\frac{3}{2}$	$-\frac{1}{2}0\frac{3}{2}$
a_F (Å)	5.75	5.71	6.15	5.53	5.63	5.67	5.45	5.75
b_F (Å)	5.61	5.59	4.97	5.80	5.65	5.64	5.65	5.65
c_F (Å)	5.59	5.49	5.88	5.55	5.54	5.44	5.71	5.49
V_F (Å^3)	180.3	175.2	179.8	178.0	176.2	174.2	175.8	178.3

Average fluorite cubic sub-cell: $V = 177.3$ Å^3 giving $\bar{a}_F = 5.62$.

Oxides belonging to this Bi_2O_3–MoO_3 and related systems, have been revealed as good ionic conductors [4–14] or catalysts [15–17]. In particular, the high-temperature form of $Bi_{2/3}[Bi_{12}O_{14}](MoO_4)_5$ exhibits a rather high anionic conductivity, as revealed by impedance spectroscopy measurements, i.e. $\sigma = 20 \times 10^{-3}$ S cm^{-1} at 650 °C [2]; such important conductivity has been directly related with the evolution of fine structural details of its crystal structure versus temperature. The column $[Bi_{12}O_{14}]$ and the isolated Bi show a remarkable stability of their atomic temperature factors, while the thermal ellipsoids of the MoO_4 tetrahedra oxygens become extremely large. The disposal of these tetrahedra in the network design wavy layers suggesting that anionic conduction occurs along this two-dimensional space, a conduction being enhanced by the $\frac{1}{3}$ vacancies created by the non-stoichiometry on the isolated Bi ($Bi_{2/3}$), then creating a three-dimensional network (in the case of $Pb[Bi_{12}O_{14}](MoO_4)_5$—no vacancy—the conductivity amounts to a lower value, 10^{-3} S cm^{-1}). The $Bi_{2n+4}Mo_nO_{6(n+1)}$ family exhibits about three orders lower conductivity, so it becomes important to identify the anionic conduction mechanisms. To look for the solution of this problem is necessary to determine their crystal structure and structural relationships.

In order to understand this structural behavior, it is worth noting the role of the lone pair brought by the Bi atoms. As it has been shown in several papers, the lone pair roughly occupies the room of an oxygen, a fact illustrated in all the structures containing ns^2 elements like Tl (I), Sn to Pb (II), N to Bi (III), S to Te (IV), Br to I (V), Xe (VI) [18,19].

This paper reports on the *ab initio* determination of $Bi_{10}Mo_3O_{24}$ structure, as well as its refinement by using the Rietveld method, from the combination of X-ray and neutron diffraction powder data. Besides, the study by high resolution transmission electron microscopy (TEM) has also been carried out.

2. Experimental details

$Bi_{10}Mo_3O_{24}$ oxide (pale yellow) was synthesized by the wet-chemistry method described elsewhere [1]. A reactive precursor was previously prepared by precipitation with n-butylamine, from the suspension of the amount of MoO_3 required to obtain a Bi:Mo molar ratio of 3.33:1, in the $Bi(NO_3)_3.5H_2O$ acidic solution. The crystallization of $Bi_{10}Mo_3O_{24}$ phase was achieved by successive accumulative heating runs (6 hours) from 550 to 750 °C, in steps of 25 °C and slow cooling within the furnace, with intermediate regrinding.

Specimens for TEM experiments were prepared from ultrasonically dispersed suspensions in butanol. A drop of each corresponding suspension was placed on a copper grid covered with a holey carbon film. Conventional TEM has been carried out in a JEOL 2000FXII transmission electron microscope working at 200 kV and high-resolution TEM (HREM) in a field-emission JEOL 3000F transmission electron microscope with 1.7 Å structural resolution working at 300 kV.

X-ray powder diffraction data were collected on a Philips X'Pert diffractometer, fitted with a Ge(111) incident beam monochromator of the Johansson symmetric type, using Cu$K\alpha_1$ radiation ($\lambda = 1.5405929$ Å). Data were recorded between 5° and 70° (2θ), with 2θ increments of 0.01° and counting time of 20 s per step.

Neutron diffraction data were collected on the E9 high resolution powder diffractometer at BENSC nuclear reactor in the Hahn-Meitner-Institut Berlin. This instrument has a vertically focusing Ge-monochromator with high take off angle ~105° (2θ), yielding a neutron flux at the sample position about 10^5 n cm^{-2} s^{-1}. Selecting the Ge(511) reflecting plane it gave a wavelength $\lambda = 1.79834(3)$ Å, refined after calibration with Y_2O_3 standard. The measurements were performed with primary and secondary collimation $\alpha_1 = 10'$ and $\alpha_2 = 20'$, respectively. The detector bank consists of 64 collimators ($\alpha_3 = 10'$) in front of 64 ^{3}He (8 atm) single detector tubes arranged on a radius of 1050 mm. The effective height of each detector tube is 150 mm and the resulting vertical detector aperture is about 7°. The angular distance between two detectors cells is 2.5° (2θ). By step scanning this interval a diffraction pattern is obtained covering a total range of 160° (2θ). The measurements were carried out at room temperature during 32 h of total counting time by collecting patterns with step size of $7.82° \times 10^{-2}$ (2θ), while the sample (mass ~7 g) was hold in a standard cylindrical vanadium container ($\phi = 8$ mm).

Both X-ray and neutron powder diffraction data have been analyzed with the Rietveld method using the program FullProf

[20], details about the procedure for the simultaneous multi-pattern refinement of joint powder data are explained forward.

3. Results and discussion

3.1. Full ab initio structural hypothesis for $Bi_{10}Mo_3O_{24}$ structure

HREM has been used to get extra structural information in order to illuminate the structural nature of $Bi_{10}Mo_3O_{24}$. Albeit important radiation damage effects during HRTEM experiments, reasonably good images could be obtained with atomic structural information, see Fig. 1. Nonetheless, the images seem to be away from ideal Scherzer focus. Besides, due to the formation Bi_2O_3 nanocrystallites on the edges of the crystals as a byproduct of the radiation damage no good HREM images could be obtained from thin specimen areas on the edges. As a consequence, the image shown in Fig. 1 is from a relatively thick crystal and slightly far from the ideal Scherzer focus. Therefore, an intuitive interpretation of the image contrast is not straightforward since a direct correlation between dark areas of the image with atoms is not possible. Such a direct correlation is only possible at the weak phase object (WPO) approximation which occurs with very thin crystals at the Scherzer focus. Therefore, image simulation experiments were accomplished for different thicknesses and defoci using early models proposed for this phase [1] in order to understand the nature of the contrast observed. A structural interpretation of the HREM image was based on the hypothesis that large white dots were caused by empty voids surrounded by Bi atoms which keep the atomic structure of δ-Bi_2O_3 with basic fluorite-type structure. A scheme of the HREM was reconstructed (Fig. 2a) and the large white dots were "included" in Bi squares (Fig. 2b). Such hypothesis allowed to settle all the Bi atoms contained in the cell (20 atoms) leaving just groups of three "holes", subsequently attributed to Mo atoms, which were then readily fixed (Fig. 2c). A precise investigation by simulated images of the HREM image allowed to settle definitively this order between Bi and Mo atoms which can be proposed for the phase $Bi_{10}Mo_3O_{24}$. The full HREM study, extended to all the n members of the series is developed elsewhere by Landa-Cánovas et al. [21]. This solution, different from the first hypothesis depicted in the previous work [1], is illustrated in Fig. 3.

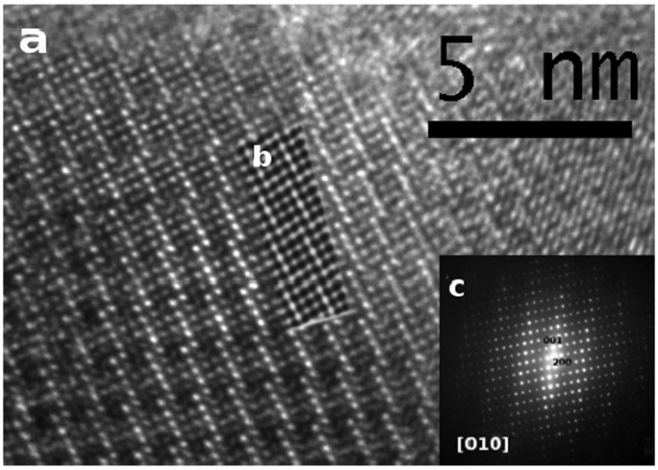

Fig. 1. (a) HREM image of a $Bi_{10}Mo_3O_{24}$ microcrystal projected along the [010] zone axis; (b) image simulation (obtained for a defocus of −100 nm and a thickness of 10 nm) is inserted in the middle of the experimental image for the cation model proposed in Fig. 3; (c) corresponding selected area electron diffraction pattern.

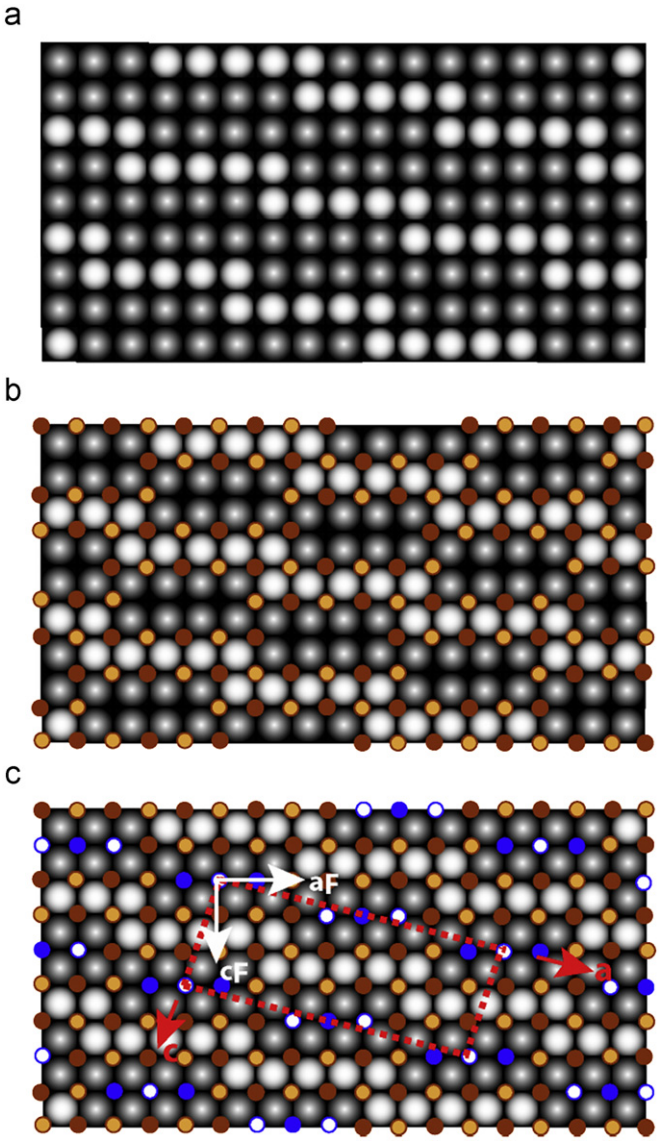

Fig. 2. (a) Schematic representation of $Bi_{10}Mo_3O_{24}$ HREM image; (b) Bi atoms (brown circles) inserted in order to surround the HREM whitest dots; (c) insertion of Mo atoms (blue circles) to complete the heavy atoms fluorite network and drawing of the cell. There are 20 Bi and 6 Mo in the cell, perfectly ordered, in agreement with the $C2$ space group. [For interpretation of the references to color in this figure legend, the reader is referred to the webversion of this article.]

With such order of the heavy atoms, the simulated X-ray powder pattern shows better agreement with the experimental one than previously reported [1]. However, it is known that in such structures, having a strong fluorite sub-lattice of heavy atoms, the oxygen contribution to the X-ray powder diffraction pattern is weak and not easily distinguishable without good single crystals, by contrast to the neutron case. Thus the only way to determine the structure by allocating the 48 oxygen atoms per unit cell was to perform a neutron diffraction experiment. For the refinement it is necessary a starting model close to the real structure, then it was decided to try to elaborate an *ab initio* structural hypothesis only by using crystal chemistry principles.

The coordinates of the heavy elements were roughly estimated on the paper using a decimeter and a pocket computer. The y coordinates were according $C2/m$ space group $y = 0$ and $\frac{1}{2}$. Therefore it was difficult to keep this space group, with mirror planes, owing to the presence of MoO_4 tetrahedra. So, the space

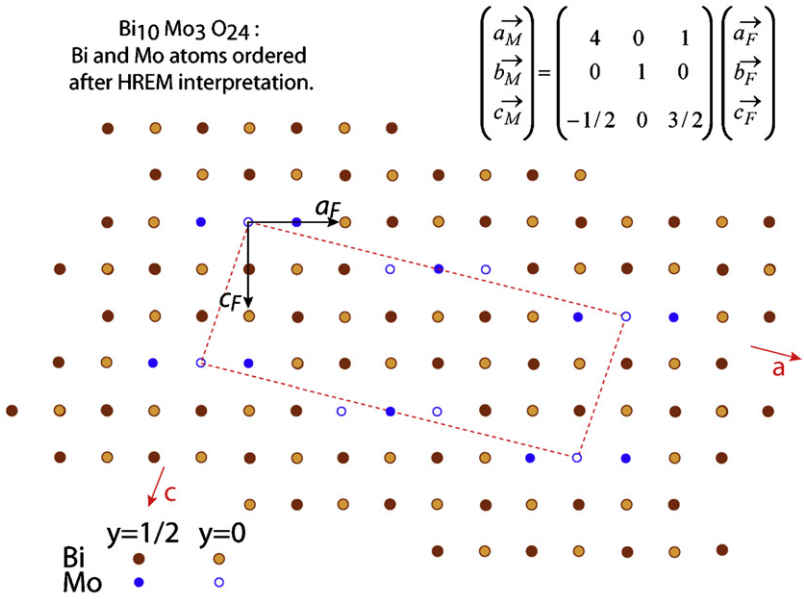

Fig. 3. Bi and Mo atoms in $Bi_{10}Mo_3O_{24}$ arranged alike in a fluorite type cell. The matrix gives the relation between basic fluorite structure and $Bi_{10}Mo_3O_{24}$ superstructure.

group *C*2 was preferred with $y \sim 0$ and $\frac{1}{2}$ for the heavy atoms. The coordinates of Bi and Mo are given in Table 2: five Bi (Bi1 to Bi5), one Mo1 in Wyckoff 4*c* and one Mo2 in Wyckoff 2*a*, in order to complete the set of heavy atoms for the two $Bi_{10}Mo_3O_{24}$ formula per cell.

It was postulated that the MoO_4 tetrahedra, alike in the high temperature form $Bi_{2/3}[Bi_{12}O_{14}](MoO_4)_5$, might be rather independent. It means six sets of independent (*xyz*) oxygen coordinates, two O around Mo2 sitting on the twofold axis in Wyckoff 2*a* and four O around Mo1 in Wyckoff 4*c*, in order to complete the six (MoO_4) tetrahedra of the cell, i.e. 24 oxygens. Such hypothesis implies to find the oxygen coordinates generating the remaining 24 oxygens linked to Bi atoms. That was the estimated priority.

To find the coordinates of these oxygens within the Bi network, we recall the structure of the $[Bi_2O_2]_n$ layer in BiOF or Aurivillius phases, which is very similar to the well known structure of red PbO. A projection of PbO along the [110] crystallographic direction is given in Fig. 4. It is worth noting that the sequence of heavy atoms is the same: Bi or Pb are fourfold coordinated to oxygen and exhibit, taking into account the lone pair (E), the well known square pyramid (SP) BiO4E, that is to say, coordination number CN = 4+1. A picture is included in Fig. 4.

Starting with such kind of coordination scheme for Bi for the $Bi_{10}Mo_3O_{24}$ phase, the introduction of 12 oxygens was done between the rows of Bi atoms. The estimated y coordinates were settled around 0.25 and 0.75. This preliminary structure hypothesis is illustrated in Fig. 5.

Oxygen atoms O5 and O6 in the projected square Bi4Bi5Bi4a-Bi5a are placed on to the twofold axis, Wyckoff 2*b*, at coordinates $z \sim 0.25$ and 0.75, respectively. O3 and O4 in the projected square Bi2Bi3Bi5Bi4 are in Wyckoff 4*c*, again at coordinates $z \sim 0.25$ and 0.75. Such atomic positions give rise to 20 oxygen atoms placed in the cell. According the statement indicated above four oxygens remain to be added. O7 aligned with the oxygen planes was introduced in the "square" Bi1bBi2Bi4Mo1b in a 4*c* Wyckoff site, with $z \sim 0.25$. With such primary approach all the 24 oxygens linked to Bi atoms were settled.

To achieve the full content of the cell, i.e. two formula units $Bi_{10}Mo_3O_{24}$ or $2\{[Bi_{10}O_{12}](MoO_4)_3\}$, three MoO_4 groups remain to be located. According to Fig. 5, the depicted green circles centered onto the Mo atoms give the space in which such oxygens should be located. Around Mo1 four oxygens in Wyckoff position 4*c*, O8, O9, O10 and O11, were settled taking into account the classical Mo–O bonds and the inter-atomic distances to other oxygens and bismuth atoms. The two remaining oxygen positions in 2*a* around Mo2 atom, the only heavy atom situated onto the twofold axis, were then postulated in a similar way, i.e. O12 and O13.

All the atomic positions from this *ab initio* structural hypothesis for the $Bi_{10}Mo_3O_{24}$ compound are summarized in Table 2. On

Table 2
Atomic positions in monoclinic space group *C*2 and isotropic temperature factors $B(Å^2)$ of $Bi_{10}Mo_3O_{24}$ obtained from simultaneous Rietveld refinement of X-ray and neutron powder diffraction data. Calculated bond valence sums (BVS) in valence units are included for each atom in the asymmetric unit. Reliability factors and lattice parameters are given below.

Atoms	Multiplicity Wyckoff	*x*	*y*	*z*	B(Å^2)	BVS (*v.u.*)
Bi1	4*c*	0.2403(3)	0.035(2)	0.8113(7)	0.40(3)	3.22(7)
Bi2	4*c*	0.3073(3)	1.089(2)	0.4559(8)	0.40(3)	2.86(6)
Bi3	4*c*	0.1465(3)	0.037(2)	0.2434(8)	0.40(3)	2.87(5)
Bi4	4*c*	0.0768(3)	1.015(3)	0.5944(7)	0.40(3)	2.98(5)
Bi5	4*c*	0.4624(3)	0.013(3)	0.6768(8)	0.40(3)	3.19(6)
Mo1	4*c*	0.3747(4)	0.055(2)	0.0754(9)	0.47(12)	5.50(12)
Mo2	2*a*	0	0	0	0.47(12)	5.88(11)
O1	4*c*	0.2218(4)	0.250(3)	0.311(1)	0.72(8)	2.06(5)
O2	4*c*	0.2224(5)	0.763(3)	0.349(1)	0.72(8)	2.21(5)
O3	4*c*	0.1025(5)	0.243(3)	0.406(1)	0.72(8)	2.19(5)
O4	4*c*	0.1072(5)	0.747(3)	0.430(1)	0.72(8)	2.12(5)
O5	2*b*	0	0.324(4)	$\frac{1}{2}$	0.34(19)	2.26(5)
O6	2*b*	0	0.797(4)	$\frac{1}{2}$	0.34(19)	1.95(4)
O7	4*c*	0.3239(5)	0.439(3)	0.359(1)	1.57(23)	2.21(6)
O8	4*c*	0.3304(5)	0.293(3)	1.014(1)	1.71(11)	1.85(8)
O9	4*c*	0.3265(5)	0.860(3)	0.166(1)	1.71(11)	1.74(6)
O10	4*c*	0.4273(5)	0.125(3)	0.233(1)	1.71(11)	1.73(6)
O11	4*c*	0.3956(5)	0.870(3)	0.916(1)	1.71(11)	1.67(6)
O12	4*c*	0.4407(5)	0.316(3)	0.949(1)	1.62(15)	1.80(6)
O13	4*c*	0.5076(6)	0.666(3)	0.832(1)	1.62(15)	1.90(5)

$a = 23.7282(2)$ Å, $b = 5.64906(6)$ Å, $c = 8.68173(9)$ Å, $\beta = 95.8668(7)^\circ$, $V = 1157.62(1)$ Å^3, $Z = 2$, $\rho = 7.926\,g\,cm^{-3}$.
Neutron background corrected factors: $R_p = 8.08\%$, $R_{wp} = 9.03\%$. Global weighted: $R_B = 4.97\%$, $R_F = 3.21\%$.

this base a careful Rietveld refinement of joint X-ray and neutron data has been performed. No attempts were made to find a structural model with automatic calculation procedures like those based on DFT (density functional theory). Although some results on more simple related phases, like $Bi_{14}MoO_{24}$ with tetragonal cell and less crystallographic positions have been reported [22].

3.2. X-ray and neutron diffraction data analysis

3.2.1. Weighting scheme

Provided that single crystals of $Bi_{10}Mo_3O_{24}$ are not available, the only way to determine its crystal structure was a multi-technique approach combining HRTEM, electron, X-ray and remarkably neutron powder diffraction, the last one being the only scattering technique able to locate the oxygen atomic coordinates and to provide reliable temperature factors in such a case. As we have mentioned X-ray powder pattern is strongly dominated by the scattering from the heavy elements Bi and Mo, even with single crystals the oxygen contribution could be quite biased by absorption and extinction effects, besides the expected low contrast for oxygen close to the heavy metals.

Nevertheless, taking into account the number of atoms of each element per unit cell volume in $Bi_{10}Mo_3O_{24}$ and the neutron scattering cross sections $\sigma = 4\pi|b|^2$ with the corresponding neutron coherent scattering lengths for these species ($b_O = 0.5803$; $b_{Bi} = 0.8532$; $b_{Mo} = 0.6715$)$\cdot 10^{-12}$ cm, it is evident that about half of the total scattered intensity in the neutron diffraction experiment comes from the oxygen sub-lattice. Moreover the different b entering into the structure factor calculations allow to distinguish between these three elements.

On the other hand we remark that neutron diffraction is the most straightforward way to determine the displacement thermal parameters of the atoms. In this sense it is worth noting that in the high 2θ diffraction angle part of the pattern there is plenty meaningful information which is not accessible by the inherent limitations of the X-ray powder diffraction.

Furthermore, the Debye-Waller temperature factors correlate $\propto(\sin\theta/\lambda)^2$ in a similar fashion as the X-ray atomic form factors decay. However the isotropic nuclear interaction of neutrons provides constant scattering lengths along the whole angular range.

Keeping in mind these arguments, in the simultaneous refinement of both patterns it was considered a factor 2 higher for the relative contribution of the neutron data. In this sense our X-ray diffraction pattern contains 6500 points step sized 0.01° and 300 reflections, while the wider 2θ neutron profile contains 2050 points separated 0.0782° and covers 897 reflections. Even other weighting schemes with higher contribution ratio for the neutron data could be also reasonable. The main three reasons to include X-ray data and perform a simultaneous fitting were: inherent better line resolution for X-ray; correlating all atoms crystallographic positions gives complementary information for the location of heavy cations Bi and Mo; the possibility of reaching a

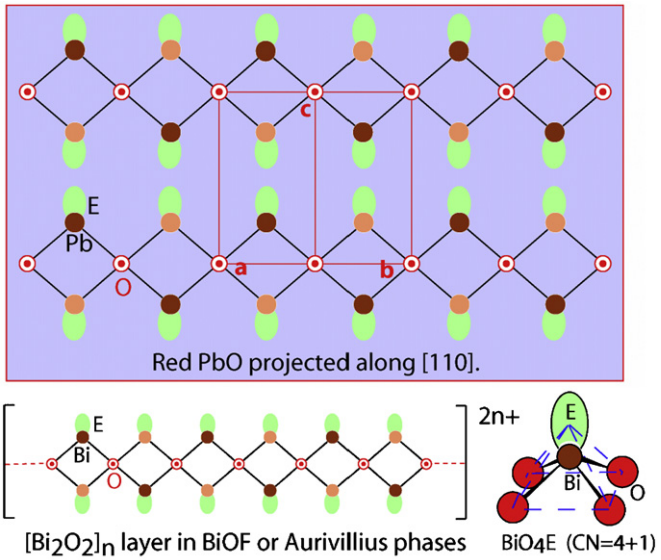

Fig. 4. Projection along [110] direction of the tetragonal red PbO and in the same direction a $[Bi_2O_2]_n$ layer. On the bottom part right square pyramid BiO_4E showing the typical coordination CN = 4+1 of Bi with its lone pair E.

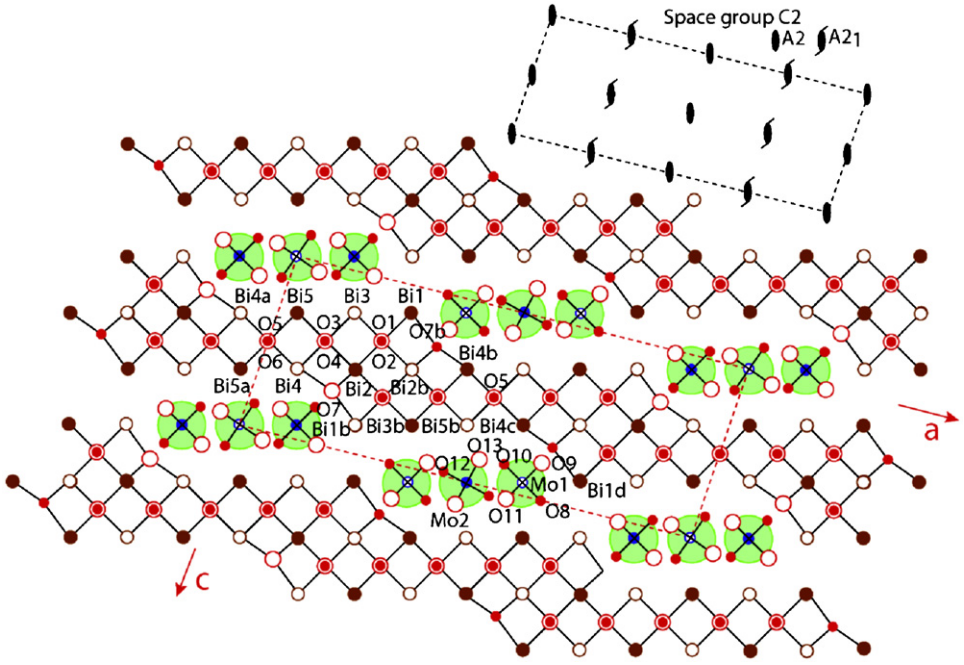

Fig. 5. Insertion of oxygen atoms O1–O7 in the Bi network of $Bi_{10}Mo_3O_{24}$ and O8–O13 around the Mo1 and Mo2 atoms to form MoO_4 tetrahedra.

local minimum (false) during least squares refinement is drastically decreased by using different data sets.

3.2.2. Refinement procedure

Contrary to single crystal structure determination, Rietveld analysis is not a structural solution method itself but a refinement procedure, so *ab initio* determination is quite a difficult task without some a priori knowledge. For $Bi_{10}Mo_3O_{24}$, even starting with an appropriate model, the refinement is not a standard case so we had to consider carefully many aspects.

About global and profile parameters we just mention that the selected peak shape functions were: a pseudo-Voigt type (linear combination of Gaussian and Lorentzian) for the X-ray data and a special pseudo-Voigt convoluted with axial divergence asymmetry function for the neutron profile.

About the intensity dependent parameters in the refinement, i.e. atomic positions and thermal factors, we should remark that the observed cell proposed from our indexation of X-ray and electron diffraction data has a rough volume $\sim$1157 Å^3 containing 74 atoms. Within our *ab initio* model suggested in Table 2, there are 20 different atomic positions in the asymmetric unit, mostly in general positions. Thus considering the restrictions of point symmetry for Wyckoff sites in *C*2 it gives rise to 53 independent atomic coordinates to refine. Later we have to add also the temperature factors.

Being possible from the extinction rules the spaces groups *C*2, *Cm* and *C*2/*m*, it is a good starting point to limit the number of parameters in the initial refinements by keeping the highest possible symmetry. So taking into account those atomic coordinates $y\sim0$ or $\frac{1}{2}$ and the multiplicity-splitting of Wyckoff sites between *C*2 and *C*2/*m*, it is possible to start with hard constraint imposed by symmetry on Bi and Mo atoms: 4*c*(*x*,*y*,*z*) to 4*i*(*x*,0,*z*); 2*a*(0,*y*,0) to 2*a*(0,0,0) and coupling the different sets of oxygens: Σ{O1, O2} or Σ{O3, O4} from 4*c* to 8*j*, and Σ{O5, O6} 2*b*(0,*y*,$\frac{1}{2}$) to 4*h* in *C*2/*m*. This technique decreases 15 free parameters, that later could be refined. As we have mentioned in Section 3.1, the space group is *C*2 and oxygens belonging to MoO_4 tetrahedra are not correlated in this initially constrained framework. However we used another setting of slack constraints (quite relaxed) commanding soft limits on some selected interatomic distances O–O ($\sim$2.8 Å$\pm$0.5) and Mo–O ($\sim$1.75 Å$\pm$0.2) to avoid unrealistic fluctuations of the parameters during the cycles of the refinement.

On feed-back to the starting model we reallocate O7 coordinates. We noticed that the shifts of the associated parameters were quite random and show high deviations, besides the correct O7 position influences strongly the intensity of the reflection (001) which was underestimated by the initial model. This checking allowed us to improve its position, initially far by $\sim$6 Å to the right one, its "hole" in fact is occupied by Bi1 lone pairs pointing towards each other.

After refining by steps all sets of (*x*,*y*,*z*) coordinates free on *C*2 and the isotropic temperature factors (which have been correlated by groups of chemically and crystallographically related atoms) the convergence is reached with very good reliability factors (weighted $R_B = 4.97\%$; $R_F = 3.21\%$) [23]. The agreement between observed and calculated patterns is plotted in Fig. 6 for both neutron and X-ray diffraction data. The results of the refinement are displayed on Table 2 and the interatomic distances and selected angles obtained from these positions and lattice parameters are shown in Tables 3 and 4. We remark that these bond lengths are not hard constrained but the results of the refinement guided using soft restrain. The same solution is achieved and keeps stable by removing all distance constraints once convergence has been reached at the end of the refinement or in the final cycles before refining the atomic B_{iso}. Based on these detailed results we discuss below some of the most striking features of the structure.

3.3. Structure description

The $Bi_{10}Mo_3O_{24}$ refined structure projected onto (010) plane is shown in Fig. 7. The general structure is built up by $\{Bi_{10}O_{12}\}_n$ puckered layers parallel to the (001) plane formed in projection by a group of five "pseudo-squares" of Bi atoms making a disruption by edge sharing at the level of Bi2Bi2b. These layers are separated by groups of three MoO_4 tetrahedra centered on the Mo2 atoms settled in the [001] direction on twofold axes with a period *a*/2. The Bi and its associate lone pair (E) shows three type of oxygen coordination within the $[Bi_{10}O_{12}]_n$ layers: CN 3+1 tetrahedron (T) BiO_3E, CN 4+1 trigonal bipyramid (TBP) BiO_4E and CN 4+1 SP BiO_4E. The details of the bond distances and angles are summarized in Table 3 and the schematic shape of these groups in Fig. 8. These BiO_nE polyhedra sharing edges and corners build the $[Bi_{10}O_{12}E_{10}]_n$ layers. The different Bi–O bond lengths range between ca. 2.1 and 2.5 Å.

Mo1 and Mo2 exhibit Mo–O bonds in excellent agreement with classical values with an average distance, Mo1–O = 1.80$\pm$0.03 Å and Mo2–O = 1.76$\pm$0.01 Å. The bond angles O–Mo–O differ just around 1°–9° from the perfect tetrahedral angles, see Table 3.

The $Bi_{10}Mo_3O_{24}$ structure shows a remarkable organization when Bi lone pairs are added. Between the $[Bi_{10}O_{12}E_{10}]_n$ layers which pack parallel to (001) plane the blocks of three MoO_4 groups, appear surrounded by lone pairs making a close channel (highlighted by a violet line in Fig. 7) developed along the [010] direction.

The most striking feature of this structure is the existence of a new type of puckered $\{(Bi_{10}O_{12})^{6+}\}_p$ layers, their charge being balanced by $\{3\{MoO_4\}^{2-}\}_p$ tetrahedra groups. This puckered layer may be derived from an Aurivillius $\{Bi_2O_2\}_n$ layer by a crystallographic shear (CS), occurring every five Bi along [100], with a slip along [001] two Bi squares sharing an edge in that direction. A scheme of such CS and reconstruction is illustrated in Fig. 9, a CS being induced by the presence of extra oxygens in this layer. Having this in mind, the most adequate formula for the whole $Bi_{2(n+2)}Mo_nO_{6(n+1)}$ series becomes $\{(Bi_{2n+4}O_{2n+6})(MoO_4)_n\}$, in such a way that for $n = 3$, 4, 5 and 6, the CS occur every 5, 6, 7 and 8 Bi along [100], respectively, i.e. every (*n*+2) Bi. Notice that $n = 1$ (Bi_6MoO_{12}) and $n = 2$ ($Bi_8Mo_2O_{18}$) members are not known. However, the member for, lets say $n = \infty$ should have as composition Bi_2MoO_6 and would consist of a pseudo-Aurivillius structure composed of an infinite Bi_2O_2 layer intergrown with an infinite layer of MoO_4 tetrahedra. There exists the Bi_2MoO_6 phase but it exhibits a real Aurivillius structure where the molybdenum oxide layer consists of corner-connected MoO_6 octahedra instead of independent MoO_4 tetrahedra.

3.4. Structural details and relation to properties

We have shown that the structure exhibits typical coordination scheme of Bi^{3+}, from CN = 3+1 T to 4+1 with both types TBP and SP. Such stereochemistry with similar bond length and angles are found in the crystal networks of phases like $Pb[Bi_{12}O_{14}](MoO_4)_5$ [24], $Bi_{2/3}[Bi_{12}O_{14}](MoO_4)_5$, $Bi[Bi_{12-x}Te_xO_{14}]Mo_{4-x}V_{1+x}O_{20}$ [25], Bi_2MoO_6 [26], $Bi_{14}P_4O_{31}$, $Bi_{50}V_4O_{85}$ [27] or $Bi_{7-x}As_{1+x}Mo_3O_{21}$ [10]. Regarding Mo^{6+}, it shows typical values in its fourfold coordination with oxygens. The tetrahedra are not too much distorted, being more regular $Mo(2)O_4$ than $Mo(1)O_4$ (see angles and distances in Table 3). On the other hand, the observed interanionic distances O–O amount reasonable values taking into

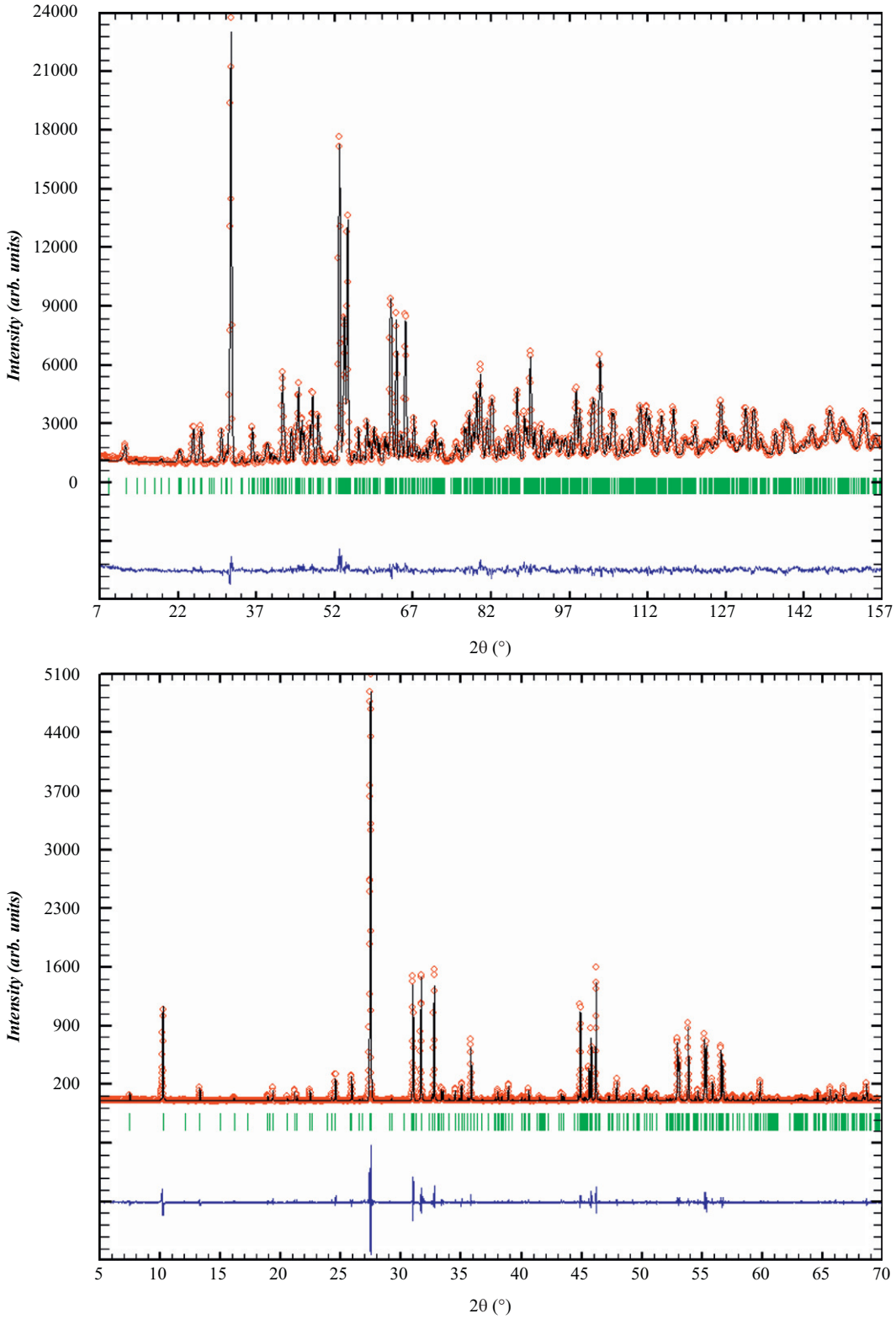

Fig. 6. $Bi_{10}Mo_3O_{24}$ powder diffraction patterns: neutron data (upper figure) and X-ray data (lower figure). Both have been refined simultaneously using the Rietveld method. Open dots are the experimental counts; continuous line is the calculated profile; difference line is shown at the bottom of each plot; vertical marks are the allowed Bragg reflections. Reliability factors are shown in Table 2.

account the classical radius for O^{2-} $r\sim1.40$ Å [28], these distances are shown in Table 4 for O–O below 3 Å.

To look in some more detail for the structural features in $Bi_{10}Mo_3O_{24}$, we have analyzed the bond length distances shown in Tables 3 and 4 using the bond valence method [29–31]. In this way, the bond valence sums (BVS) calculated for the different atoms in $Bi_{10}Mo_3O_{24}$ are shown in Table 2, their values indicate some deviation to formal oxidation states that accounts for special features in this compound. Thus regarding the metallic framework, Bi BVS agree well with the expected value 3+ within

Table 3
Bond lengths metal-oxygen and angles in the various coordination polyhedra of $Bi_{10}Mo_3O_{24}$ obtained from simultaneous refinement of X-ray and neutron powder diffraction data.

CN around Bi atom	Bi–O distance (Å)	O–Bi–O angle (deg)
Bi1 CN3+1 Tetrahedron	Bi1–O1 2.170(17) Bi1–O2 2.157(16) Bi1–O7 2.083(14)	O1–Bi1–O2 84.8(1.1) O2–Bi1–7 90.8(1.0) O1–Bi1–O7 76.7(8)
Bi2 CN4+1 Trigonal bipyramid (TBP)	Bi2–O1 ax. 2.451(14) Bi2–O4 ax. 2.341(16) Bi2–O2 eq. 2.136(15) Bi2–O7 eq. 2.202(19)	O1–Bi2–O4 ax. 135.4(8) O2–Bi2–O7 eq. 88.6(9)
Bi4 CN4+1 Trigonal bipyramid (TBP)	Bi4–O6 ax. 2.283(15) Bi4–O7 ax. 2.387(14) Bi4–O3 eq. 2.214(16) Bi4–O4 eq. 2.250(18)	O6–Bi2–O7 ax. 134.6(8) O3–Bi2–O4 eq. 78.0(1.0)
Bi3 CN4+1 Square pyramid (SP)	Bi3–O1 2.186(16) Bi3–O2 2.479(17) Bi3–O3 2.176(15) Bi3–O4 2.547(17)	O1–Bi3–O3 fac. 88.0(8) O3–Bi3–O4 fac. 72.6(9) O4–Bi3–O2 fac. 70.2(7) O2–Bi3–O1 fac. 72.6(9) O1–Bi3–O4 mer. 121.8(1.0) O2–Bi3–O3 mer. 118.1(1.0)
Bi5 CN4+1 Square pyramid (SP)	Bi5–O3 2.234(17) Bi5–O4 2.239(17) Bi5–O5 2.139(13) Bi5–O6 2.449(17)	O6–Bi5–O5 fac. 70.8(1.1) O5–Bi5–O3 fac. 75.7(7) O3–Bi5–O4 fac. 79.4(1.0) O4–Bi5–O6 fac. 69.8(7) O3–Bi5–O6 mer. 121.9(1.1) O4–Bi5–O5 mer. 110.0(1.1)
CN around Mo atom	**Mo–O distance (Å)**	**O–Mo–O angle (deg)**
Mo1 CN4 Tetrahedron	Mo1–O8 1.758(19) Mo1–O9 1.827(17) Mo1–O10 1.796(15) Mo1–O11 1.839(17)	O8–Mo1–O9 102.4(1.4) O8–Mo1–O10 114.3(1.2) O8–Mo1–O11 113.8(1.4) O9–Mo1–O10 102.9(1.2) O9–Mo1–O11 102.0(1.1) O10–Mo1–O11 118.4(1.2)
Mo2 CN4 Tetrahedron	Mo2–O12 1.771(14) Mo2–O13 1.758(13)	O12–Mo2–O12 108.0(1.1) O12–Mo2–O13 104.6(1.3) O12–Mo2–O13 112.0(1.2) O13–Mo2–O13 115.5(1.1)

Table 4
Interatomic distances (<3 Å) between anions and remaining metal-oxygen not taken into account for the coordination polyhedra description. Obtained from simultaneous refinement of X-ray and neutron powder diffraction data of $Bi_{10}Mo_3O_{24}$.

O–O distance (Å)		Met.–O distance (Å)	
O1–O2 2.772(23)	O7–O9 2.909(21)	Mo1–O12 2.483(17)	Bi4–O5 2.595(17)
O1–O2 2.917(23)	O8–O9 2.790(22)	Bi1–O8 2.740(16)	Bi4–O10 2.677(19)
O1–O7 2.642(17)	O8–O10 2.986(18)	Bi1–O9 2.445(18)	Bi4–O13 2.894(15)
O2–O4 2.891(17)	O8–O12 2.734(18)	Bi2–O1 2.920(17)	Bi5–O10 2.729(14)
O3–O4 2.811(23)	O9–O10 2.833(19)	Bi2–O2 2.814(17)	Bi5–O11 2.857(15)
O3–O4 2.856(23)	O9–O11 2.851(17)	Bi2–O9 2.908(15)	Bi5–O13 2.555(19)
O3–O5 2.682(12)	O10–O12 2.734(18)	Bi3–O8 2.726(16)	
O3–O11 2.894(16)	O11–O12 2.738(23)	Bi3–O11 2.485(18)	
O4–O6 2.690(13)	O12–O12 2.863(17)	Bi3–O12 2.816(15)	
O4–O7 2.568(18)	O12–O13 2.794(21)		
O5–O6 2.980(29)	O12–O13 2.925(20)		
O5–O6 2.669(29)	O13–O13 2.974(16)		
O6–O10 2.914(14)			

maximum deviation from −4% to +7%, while Mo are slightly underbonded by −8% for Mo1 and −2% for Mo2 respect expected formal valence 6+.

Regarding the anion net, two distinct groups are clearly observed. Those oxygen atoms bonded to Bi (O1–O7) show generally overbonding ranging from +2% to +13% compared to oxidation number. On the contrary oxygens belonging to MoO_4 tetrahedra (O8–O13) are underbonded by −5% to −16%. These divergences points to mixed covalency/ionic character within $[Bi_{10}O_{12}]_n$ layers/$[MoO_4]$ units. The calculated *global instability index GII* as the root mean square of the BVS deviations for all the atoms in the asymmetric unit gives $GII = 0.214$ *v.u.* meaningful within this framework. It has been stated that *GII* values higher than ~0.2 *v.u.* could indicate some kind of strain and structural instability at room temperature [32], but it could be also that the BVS rule is not fulfilled when E lone pairs or covalency or disorder effects are present. In this sense we have observed for example *GII*~0.28 *v.u.* in mixed oxides of the type *Immm*-R_2BaCoO_5 (R = Tb, Dy, Ho, Er) which nevertheless remain as stable phases during years at RT [33], however they show too the most stable polymorphs *Pnma*-R_2BaCoO_5 with more ionic character and lower *GII*~0.08 *v.u.* [34].

It is worth remarking that in fact $Bi_{10}Mo_3O_{24}$ shows higher agreement between BVS and oxidation states if we compare the values in Table 2 to that for other related Bi–Mo oxides. In this sense, by performing a calculation of *GII* for the BVS reported for $Bi_{26}Mo_{10}O_{69}$ [35] or $Bi_{26.4}Mo_{9.6}O_{68.4}$ [5] we obtain for these phases much higher *GII* values, ranging from 0.376 to 0.310 *v.u.* depending on oxygen stoichiometry and distances constraints are considered or not. This may be compared to the $GII = 0.214$ *v.u.* calculated for $Bi_{10}Mo_3O_{24}$ in this work, and might indicate possible higher structural stability and/or higher degree of order in $Bi_{10}Mo_3O_{24}$ compared to those Bi/Mo poorer ratio high T compounds. It must be noticed that composition of those reported phases approaches our low temperature stoichiometric phase of the series with $n = 6$ $Bi_8Mo_3O_{21}$. Studying the variation of the *GII* within the $Bi_{2(n+2)}Mo_nO_{6(n+1)}$ family based on accurate bond distances obtained from neutron diffraction data could seed some light on the evolution of the stability going from the rich end Bi/Mo ($n = 3$) to poorer $n = 6$, and eventually explains the reason why phases with higher or lower n values have not been observed so far.

Keeping some caution within the limitations of the data, it is also worth noting about the thermal parameters trends shown in Table 2. Marked differences have been found between the isotropic temperature factors for oxygen atoms bonded to Bi and those linked to Mo. The former shows lower values pointing to less relevant atomic displacements around the equilibrium position shown by its coordinates in Table 2. However the latter show much larger values, it should be related with the anionic conductivity already observed in this compound [1,3], remarking that the mechanism involves O^{2-} from the MoO_4 tetrahedra.

A special case is O7, its B_{iso} value is close to that found for the ones bonded to Mo (O8–O13) and being by far the highest observed displacement for oxygens within the $[Bi_{10}O_{12}]_n$ framework (O1–O7). It could be explained taking into account the structure, see Fig. 7. It is noticeable that oxygen atoms surrounded by Bi lone pairs show higher B_{iso} than those non-interacting, i.e. Mo–O respect Bi–O. However O7 shows a closer distance to the tetrahedral moieties than (O1–O6) to (O8–O13) generally well above 3 Å. In this sense O7–O9 distance amount ~2.91(2) Å, see Table 4. The tunnel composed by $[MoO_4]_3$ along [010] shown in Fig. 7 displays a longer distance Bi1–Bi4 and correspondingly less shielding by Bi electronic clouds just close to O7 position. In this "channel door" O7 and O9 show similar x coordinate.

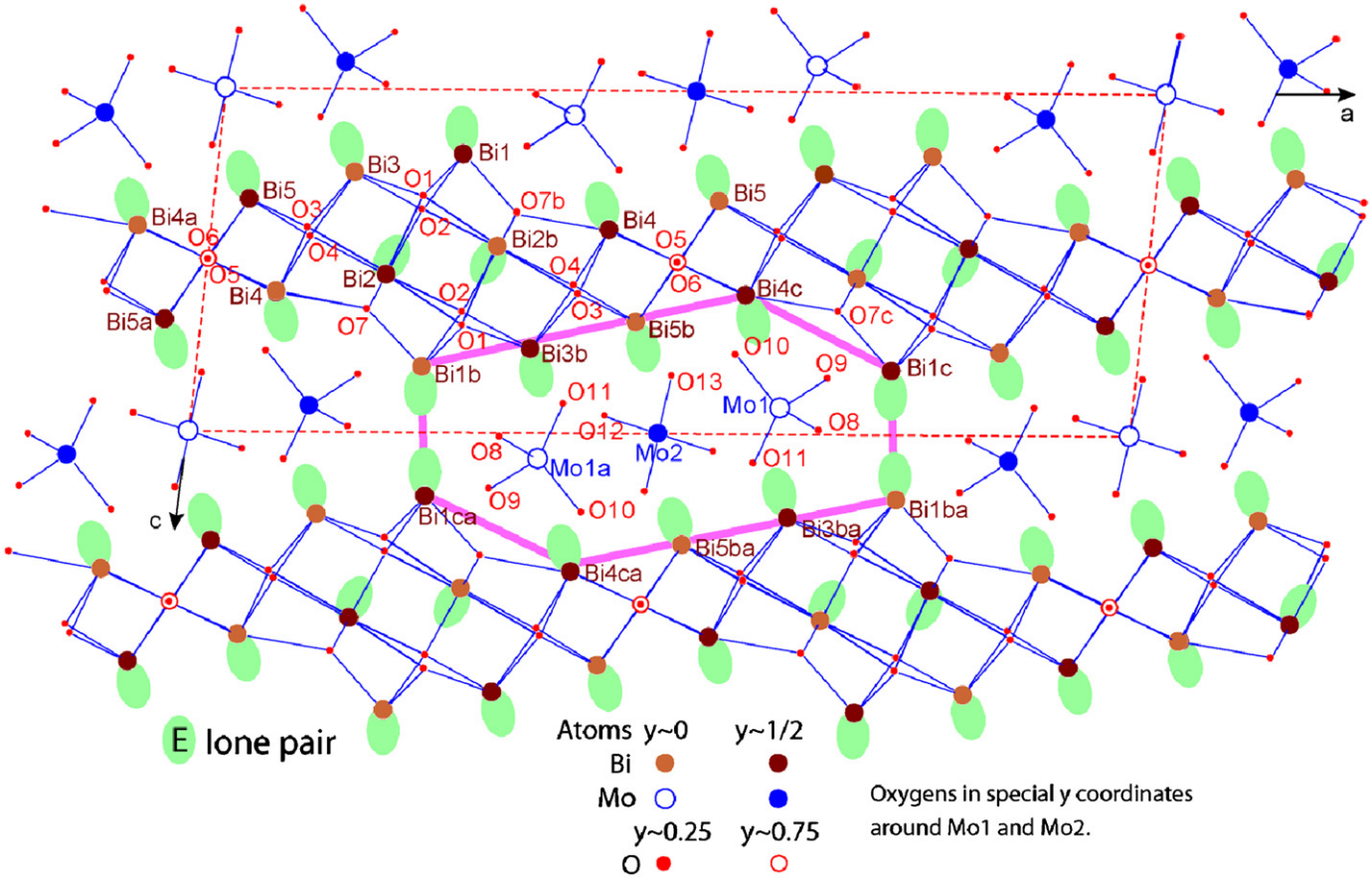

Fig. 7. Projection of $Bi_{10}Mo_3O_{24}$ refined crystal structure on to (010) plane. The channel along [010] bordered by the Bi lone pairs in which are inserted the groups of three MoO_4 tetrahedra is represented surrounded by violet lines.

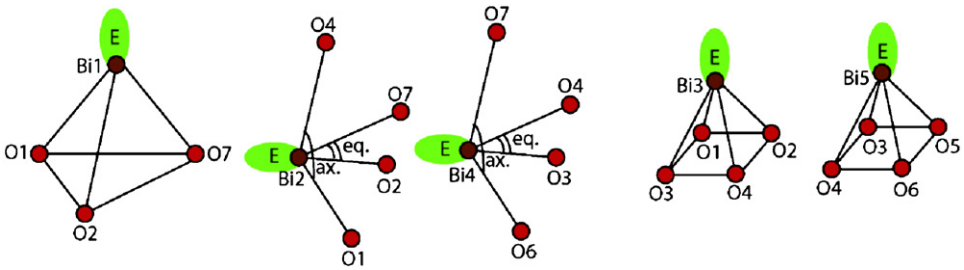

Fig. 8. Ideal scheme of the Bi respective coordination polyhedra: CN = 3+1 tetrahedron for Bi1, CN = 4+1 trigonal bipyramid for Bi2 and Bi4, CN = 4+1 square pyramid for Bi3 and Bi5.

On the other hand, even much higher B_{iso} have been found for O within MoO_4 in related compounds $Pb[Bi_{12}O_{14}](MoO_4)_5$ and $Bi_{2/3}[Bi_{12}O_{14}](MoO_4)_5$ than those in $Bi_{10}Mo_3O_{24}$. In this sense previous papers have shown that the anionic conductor behavior of the low-temperature $Bi_{10}Mo_3O_{24}$ phase is quite similar to that of L-$Bi_6Mo_2O_{15}$ [36] and $Bi_6Cr_2O_{15}$ [7], although its conductor quality is about 10^2 times lower than that of the corresponding high-temperature form [36]. This fact could be now understood on the basis of the determined crystal structure, where the groups of three MoO_4 tetrahedra inserted in channels along [010] and bordered by lone pairs, establish its one-dimensional character from their packing, see Fig. 7. Even with a thermal activation it seems difficult that any anionic exchanges can take place between the triple MoO_4 groups, leading only a one-dimensional diffusion path possible. Such structural organization explains the lower conductivity compared to the two-dimensional one of $Pb[Bi_{12}O_{14}](MoO_4)_5$ and the best three-dimensional one of the vacancy compound $Bi_{2/3}[Bi_{12}O_{14}](MoO_4)_5$.

4. Conclusions

In summary we have determined the complex structure of $Bi_{10}Mo_3O_{24}$ oxide by *ab initio* simultaneous Rietveld analysis of X-ray and neutron powder diffraction data. The starting model was built with crystal chemistry arguments for the oxygen sublattices and supported by HRTEM and electron diffraction regarding the metallic framework.

This compound represents the first member of the series $Bi_{2n+4}Mo_nO_{6n+6}$. The net of $Bi_{10}Mo_3O_{24}$ structure is built up by $\{Bi_{10}O_{12}\}$ layers, which run parallel to (001) plane, being surrounded by groups of three isolated MoO_4 tetrahedra. These

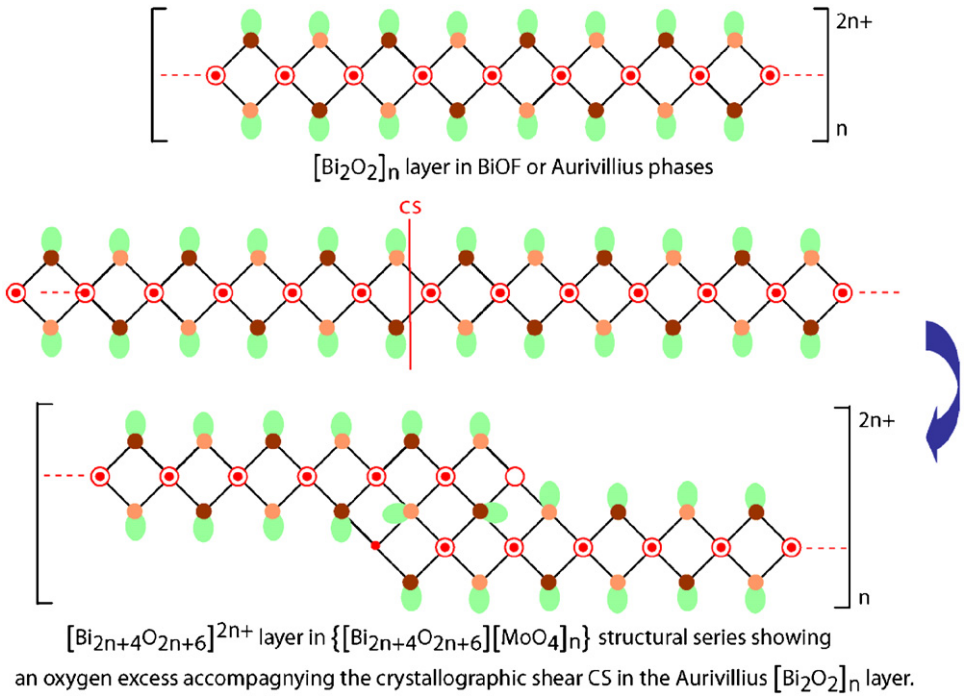

Fig. 9. Scheme of the construction of the new type of $\{Bi_{2n+4}O_{2n+6}\}_n$ layers via a crystallographic shear occurring in the Aurivillius $\{Bi_2O_2\}_n$ layer every $(n+2)$ Bi along [100].

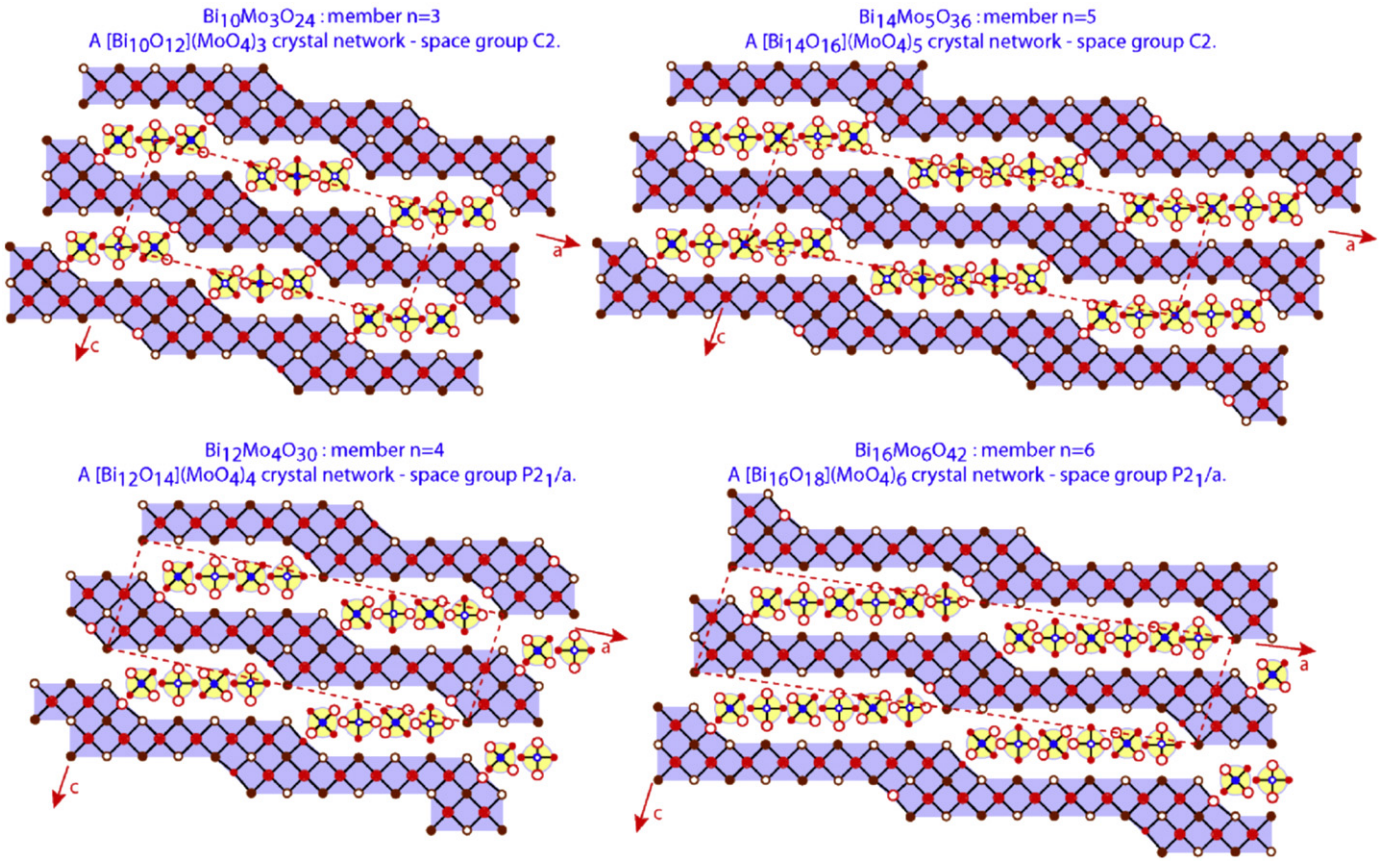

Fig. 10. Idealized representation of the whole series $Bi_{2(n+2)}Mo_nO_{6(n+1)}$ projected on to the [010] plane, in which groups of $n MoO_4$ tetrahedra are intercalated between puckered planes $\{(Bi_{(2n+4)}O_{(2n+6)})\}$.

$\{Bi_{10}O_{12}\}$ puckered layers may be seen as derived from the classical Aurivillius-type $\{Bi_2O_2\}$ one, by a crystallographic shear and a subsequent slip.

The determination of the $Bi_{10}Mo_3O_{24}$ structure gives the key to propose the full structural evolution of this original $(Bi_{2n+4}O_{2n+6})(MoO_4)_n$ series, with $n = 3$, 4, 5 and 6. The structure of the

remainder members of the $Bi_{2n+4}Mo_nO_{6n+6}$ family could be deduced from that of $n = 3$, with the difference of the periodicity in such crystallographic shear.

In this way, the member $n = 4$ may be readily drawn on the paper, with the groups of four MoO_4 tetrahedra, $\{4\{MoO_4\}^{2-}\}_p$, intercalated between the layers $\{(Bi_{12}O_{14})^{8+}\}_p$, which can be easily derived by creating a crystallographic shear in the Bi sequence every 6 Bi. Thus, a new structure is obtained as shown in Fig. 10; the symmetry of this member changes and becomes $P21/a$. The member $n = 5$ shows an organization similar to the member $n = 3$, within the $C2$ space group, while the member $n = 6$ again belongs to the space group $P21/a$. The idealized representation of the structures allows to visualize easily the mechanism of the evolution of the $Bi_{2(n+2)}Mo_nO_{6(n+1)}$ series. Up to now intergrowths between two successive members have not been identified.

Besides, the structural characteristics of $Bi_{10}Mo_3O_{24}$ phase helps to understand the ionic conductor properties of the whole $Bi_{2n+4}Mo_nO_{6n+6}$ family of low-temperature-stable oxides, which are also related to the fluorite structural skeleton. These findings could seed some light on the structure-property relationships in the fascinating Bi_2O_3–MoO_3 system.

Acknowledgments

The authors are grateful for the financial support provided by the Centre National de la Recherche Scientifique (France) and Spanish project MAT2007–61884. One of us (J. Hernández–Velasco) thanks the Spanish Ministry of Science and Innovation for contract under Ramón y Cajal programme and the BENSC for the provision of neutron beamtime with financial support through the European Commission programme NMI3 "Neutron and Muon Integrated Infrastructure Initiative" under EU FP6 "Structuring the European Research Area: Research Infrastructures", contract RII3–CT–2003–505925.

References

[1] E. Vila, J.E. Iglesias, J. Galy, A. Castro, Solid State Sci. 7 (2005) 1369–1376.
[2] J. Galy, R. Enjalbert, P. Rozier, P. Millet, Solid State Sci. 5 (2003) 165–174.
[3] E. Vila, A.R. Landa-Cánovas, J. Galy, J.E. Iglesias, A. Castro, J. Solid State Chem. 180 (2007) 661–669.
[4] P. Begue, J.M. Rojo, R. Enjalbert, J. Galy, A. Castro, Solid State Ionics 112 (1998) 275–280.
[5] R.N. Vannier, F. Abraham, G. Nowogrocki, G. Mairesse, J. Solid State Chem. 142 (1999) 294–304.
[6] R.N. Vannier, S. Danzé, G. Nowogrocki, M. Huvé, G. Mairesse, Solid State Ionics 136–137 (2000) 51–59.
[7] J. Grins, S. Esmaeilzadeh, S. Hull, J. Solid State Chem. 163 (2002) 144–150.
[8] P. Bégué, J.M. Rojo, J.E. Iglesias, A. Castro, J. Solid State Chem. 166 (2002) 7–14.
[9] B. Bastide, R. Enjalbert, Ph. Salles, J. Galy, Solid State Ionics 158 (2003) 351–358.
[10] F. Duc, P. Rozier, P. Millet, J. Galy, Solid State Sci. 6 (2004) 897–905.
[11] J. Galy, P. Salles, Ph. Rozier, A. Castro, Solid State Ionics 177 (2006) 2897–2902.
[12] B. Muktha, T.N. Guru Row, Struct. Chem. 18 (2007) 195–202.
[13] L. Holmes, L. Peng, I. Heinmaa, L.A. O'Dell, M.E. Smith, R.N. Vannier, C.P. Grey, Chem. Mater. 20 (2008) 3638–3648.
[14] C.M.C. Vera, R. Aragón, J. Solid State Chem. 181 (2008) 1075–1079.
[15] H.-Y. Chen, A.W. Sleight, J. Solid State Chem. 63 (1986) 70–75.
[16] J.F. Bradzil, D.D. Suresh, R.K. Grasselli, J. Catal. 66 (1980) 347–367.
[17] A.M. Beale, M.T. Le, S. Hoste, G. Sankar, Solid State Sci. 7 (2005) 1141–1148.
[18] J. Galy, G. Meunier, S. Andersson, A. Aström, J. Solid State Chem. 13 (1975) 142–159.
[19] J. Galy, R. Enjalbert, J. Solid State Chem. 44 (1982) l–23.
[20] J. Rodríguez-Carvajal, Physica B 192 (1993) 55–69.
[21] A.R. Landa-Cánovas, E. Vila, J. Hernández-Velasco, J. Galy, A. Castro, submitted for publication.
[22] C.D. Ling, Physica B 385/386 (2006) 193–195.
[23] J. Hernández-Velasco, A. Lánda-Canovas, E. Vila, J. Galy, A. Castro, Acta Crystallogr. A 64 (2008) C215.
[24] R. Enjalbert, G. Hasselmann, J. Galy, Acta Crystallogr. C 53 (1997) 269–272.
[25] A. Castro, R. Enjalbert, P. Baules, J. Galy, J. Solid State Chem. 139 (1998) 185–193.
[26] D.J. Buttrey, T. Vogt, U. Wildgruber, W.R. Robinson, J. Solid State Chem. 111 (1994) 118–127.
[27] F. Mauvy, J.C. Launay, J. Darriet, J. Solid State Chem. 178 (2005) 2015–2023.
[28] R.D. Shannon, C.T. Prewitt, Acta. Crystallogr. B 25 (1969) 925–946.
[29] I.D. Brown, D. Alttermatt, Acta Crystallogr. B 41 (1985) 240–244.
[30] I.D. Brown, in: M. O'Keeffe, A. Navrotsky (Eds.), Structure and Bonding in Crystals, vol. II, Academic Press, New York, 1981, pp. 1–30 (Chapter 14).
[31] N.E. Brese, M. O'Keeffe, Acta Crystallogr. B 47 (1991) 192–197.
[32] I.D. Brown, Z. Kristallogr. 199 (1992) 255.
[33] J. Hernández-Velasco, A. Salinas-Sánchez, R. Sáez-Puche, J. Solid State Chem. 110 (1994) 321–329.
[34] J. Hernández-Velasco, A. Salinas-Sánchez, F. Fernández, R. Sáez-Puche, J. Alloys Compd. 203 (1994) 15–22.
[35] D.J. Buttrey, T. Vogt, G.P.A. Yap, A.L. Rheingold, Mater. Res. Bull. 32 (1997) 947–963.
[36] E. Vila, J.M. Rojo, J.E. Iglesias, A. Castro, Chem. Mater. 16 (2004) 1732–1739.